HAL
open science

Thermal-Electromagnetic Analysis for Driving Cycles of Embedded Flux-Switching Permanent Magnet Motors

Guangjin Li, Javier Ojeda, Emmanuel Hoang, Mohamed Gabsi, Michel Lécrivain

To cite this version:

Guangjin Li, Javier Ojeda, Emmanuel Hoang, Mohamed Gabsi, Michel Lécrivain. Thermal-Electromagnetic Analysis for Driving Cycles of Embedded Flux-Switching Permanent Magnet Motors. IEEE Transactions on Vehicular Technology, 2012, 61 (1), pp.140-151. 10.1109/TVT.2011.2177283 . hal-00663157

HAL Id: hal-00663157
https://hal.science/hal-00663157

Submitted on 26 Jan 2012

HAL is a multi-disciplinary open access archive for the deposit and dissemination of scientific research documents, whether they are published or not. The documents may come from teaching and research institutions in France or abroad, or from public or private research centers.

L'archive ouverte pluridisciplinaire **HAL**, est destinée au dépôt et à la diffusion de documents scientifiques de niveau recherche, publiés ou non, émanant des établissements d'enseignement et de recherche français ou étrangers, des laboratoires publics ou privés.

Thermal-Electromagnetic Analysis for Driving Cycles of Embedded Flux-Switching Permanent Magnet Motors

G.J. LI, *Student Member*, *IEEE*, J. OJEDA, *Member*, *IEEE*, E. HOANG, M. GABSI, *Member*, *IEEE*, and M. LECRIVAIN
SATIE, ENS CACHAN, CNRS, UNIVERSUD
61, av President Wilson F-94230 – Cachan – FRANCE
E-mail: guangjin.li@satie.ens-cachan.fr

I. Abstract

This paper presents a fast and precise electromagnetic-thermal model of a redundant dual star Flux-Switching Permanent Magnet (FSPM) motor for the embedded applications with driving cycles, e.g. Hybrid Electrical Vehicle (HEV), aerospace, etc. This model is based on a prior steady characterization by Finite Element Method (FEM) 2D of the FSPM motor via calculating the instantaneous torque, the normal and tangential components of magnetic flux density (B_r and B_θ) of each element of stator as well as rotor for different RMS current densities and different rotor positions. These results are then used in the analytical copper and iron losses models for calculating the instantaneous copper and rotor as well as stator iron losses during one driving cycle. The Lumped Parameter (LP) and Finite Element 2D transient thermal models are then carried out, in which the previously obtained instantaneous power losses are used as heat sources for calculating the temperatures of different motor parts during driving cycles. In the thermal studies, a transformation of irregular slot structure into a regular (rectangular) one is applied to simplify the calculation of winding thermal resistance. The Thermal-Electromagnetic Analysis method in this paper can also be extended for all the other applications with driving cycles. The experimental tests are carried out to validate the analytical and numerical results.

Index Terms— Flux-switching, permanent magnet (PM) motor, loss modeling, thermal resistance network, finite-element (FE) analysis.

II. Introduction

DURING recent years, the Flux-Switching Permanent Magnet (FSPM) Motors have attracted a lot of attentions of the electrical machine researchers because of their outstanding performances [1]-[3]. Generally, such machines can have high torque and power densities [4]-[5]. Thanks to a simple rotor structure that is similar to Switched Reluctance Motors, the fault tolerance capability of this kind of machines can be significantly higher than rotor mounted permanent magnet machines [6]-[7]. Moreover, since the permanent magnets are mounted on the stator, the heat due to copper and iron losses are easier to be dissipated and the cool system could be simpler. This leads that the FSPM motors can be employed in some harsh environments, e.g. high ambient temperature, high speed, etc. In order to improve the flux weakening capability of flux-switching permanent machines, the hybrid excitation flux-switching permanent machines have been studied in recent years [8]-[9].

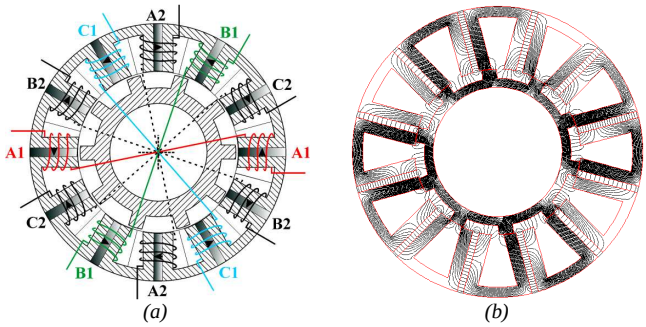

Fig. 1 Dual-star flux-switching permanent magnet motor (2×6/10) with two three phases. The phases A1, B1, C1 are primary phases, which are supplied under normal mode, while the phases A2, B2, C2 are standby phases supplied under faulty modes. (a) cross-section of the machine, (b) no-load flux distribution.

In high reliability applications such as Hybrid Electrical Vehicle (HEV) and aerospace, in order to ensure the operation continuity, a dual star flux-switching permanent magnet motor is considered in the conception process (see Fig. 1). As in [10]-[11], the two three phases of stator are supplied by two independent voltage source inverters (VSIs). In normal mode, only the primary phases (in this paper, phases A1, B1, C1 are primary phases) are supplied. To some degree, this is similar to a flux-switching permanent magnet machine with alternate poles wound [3], [12]. When a short-circuit or open-circuit occurs, in order to reduce the torque pulsation and mutual influence between phases, all the primary phases are opened, at the same time, the standby phases are supplied simultaneously and the operation continuity can be consequently ensured.

Besides the fault tolerance consideration in the conception process, it is also necessary to perform a thermal analysis to make sure that the machine can satisfy the thermal constraints. To our best knowledge, previous thermal modeling studies were often focused on one driving point of electrical machines, in which the output torque and rotor speed are constant, the heat source is considered as the sum of maximum copper and iron losses as well as mechanical losses [13]-[18]. A few studies have been reported about the electrical machines with duty cycles [19]-[22], in which the duty cycle was constant and a value of 50% was often chosen. Whereas, to the electrical machines having driving cycles as for HEV and aerospace, these kinds of method cannot be employed any longer, because it has been known that during the driving cycles, the output torque and the rotor speed are variable. As an example, an electrical machine designed for Variable Stator Vane (VSV) of aircraft engine is studied, in which the electrical machine is applied to control the open angle of vanes

so that the air flow enters in the aircraft engine can be controlled and the regime of the engine can be regulated. Thus, the variations of the average torque and the rotor speeds are considerably irregular (see Fig. 2). This leads to variable copper and iron losses. Furthermore, the maximum copper and iron losses do not appear at the same moment during a driving cycle, because the maximum torque corresponds (maximum copper losses) often to the minimum rotor speed (minimum iron losses). Thus, if the sum of maximum copper and iron losses is taken to calculate the maximum temperature, the obtained results could be significantly deviated from the real values. This could lead to no optimal dimensions in the conception process and a good candidate could be rejected. For the machines having driving cycles, the steady-state thermal analysis could be insufficient, because the maximum copper or iron loss is often during only several seconds that depends on the machine specification (in this paper, 200s for the maximum copper loss and 50s for iron loss). Thus, due to the thermal time constant of different components of the electrical machines, in transient regime, the maximum temperature could not reach the same value as that in the steady-state regime.

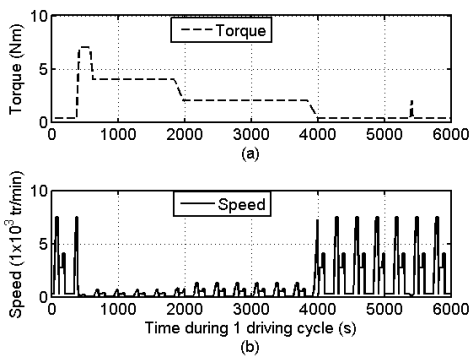

Fig. 2 The machine specifications of the dual star FSPM motor for VSV application. (a) output torque versus time during one driving cycle, (b) rotor mechanical speed versus time during one driving cycle.

Based on this example, we will establish a methodology for calculating instantaneous power losses and heating of electrical machines. This methodology will be applied to similar cases such as hybrid or electrical vehicles. This paper is organized as follows. Based on the torque and speed versus time during driving cycle (given in machine specifications), copper and iron losses for driving cycles were calculated in Section III. In order to simplify the computation of thermal resistance, the section IV proposed a novel method to transform the irregular stator structure in a regular one, and a lumped parameter thermal model was finally established. Based on the lumped parameter thermal model, the transient thermal analyses were realized and the results were verified by Finite Element Method 2D (FEM 2D) and the analytical and numerical results are also validated by experimental tests. All of this is applied for the machines with redundancy. Conclusions are finally given in the Section V.

III. Loss Model of Dual Star (2 × 3 Phase) FSPM Motor

In contrast to previous studies, where iron loss was obtained at certain driving points (output torque and rotor speed are constant) or the computation was often performed in no-load conditions [23]-[26], in this paper, the output torque corresponding to copper loss and the rotor mechanical speed corresponding to iron loss are variable during one driving cycle. Moreover, the computation of iron loss was realized in on-load condition. The characteristic parameters of the dual star FSPM motor are shown in Fig. 2. It is noticed that the maximum and minimum output torques are respectively 0.4 Nm and 6.9 Nm, and the maximum and minimum rotor speeds are 8000 tr/min and 20 tr/min, respectively. The flow chart of the coupled thermal-electromagnetic model of the FSPM motor with driving cycle for calculating the temperature evaluation during driving cycle is shown in Fig. 4. The machine parameters for realizing all the computations are given in the appendix. The copper losses (P_j) in primary stator winding can be computed as

$$P_j = \rho \cdot J_{RMS}^2 \cdot V_{cu} \tag{1}$$

Where ρ (Ωm) is the copper resistivity, J_{RMS} (A/m^2) is the RMS current density, which dependents on the output torque and can be obtained by FEM 2D [see Fig. 3 (b)], V_{cu} (m^3) is the total copper volume of primary winding. With the characteristic B-H of the Fe-Co 50 for the stator and rotor cores [see Fig. 3 (a)], the average torque versus RMS current density [T_{em} (J_{RMS})] can be obtained. Using the MATLAB based Basic-Fitting, an analytical relationship between the average torque and the RMS current density can be established [$J_{RMS}=f^{-1}(T_{em})$]. With the torque versus time during one driving cycle [T_{em} (t)] [see Fig. 2 (a)] and the expression (1), the copper losses during one driving cycle [P_j (t)] can be finally obtained.

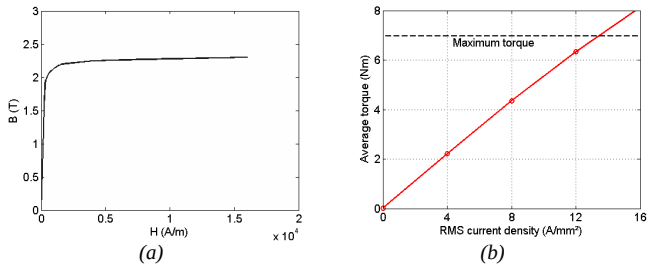

Fig. 3 B-H curve of Fe-Co 50 and the average torque versus RMS current density obtained by FEM 2D. 6.9 Nm is the maximum torque of in the machine specification.

In this paper, the magnetic flux densities (B) in different mesh elements of stator and rotor were obtained by time-stepping Finite Element Method (FEM) 2D (the form of mesh elements is triangular, see fig. 13). The time derivative of flux density was calculated from normal and tangential components (B_r and B_θ) with the relationship (2) [25]. For a driving cycle, the magnetic flux densities of all the mesh elements of the motor, the number of which is n, are considered as functions of the RMS current density as well as the rotor position [B_r (θ, J_{RMS}), B_θ (θ, J_{RMS})].

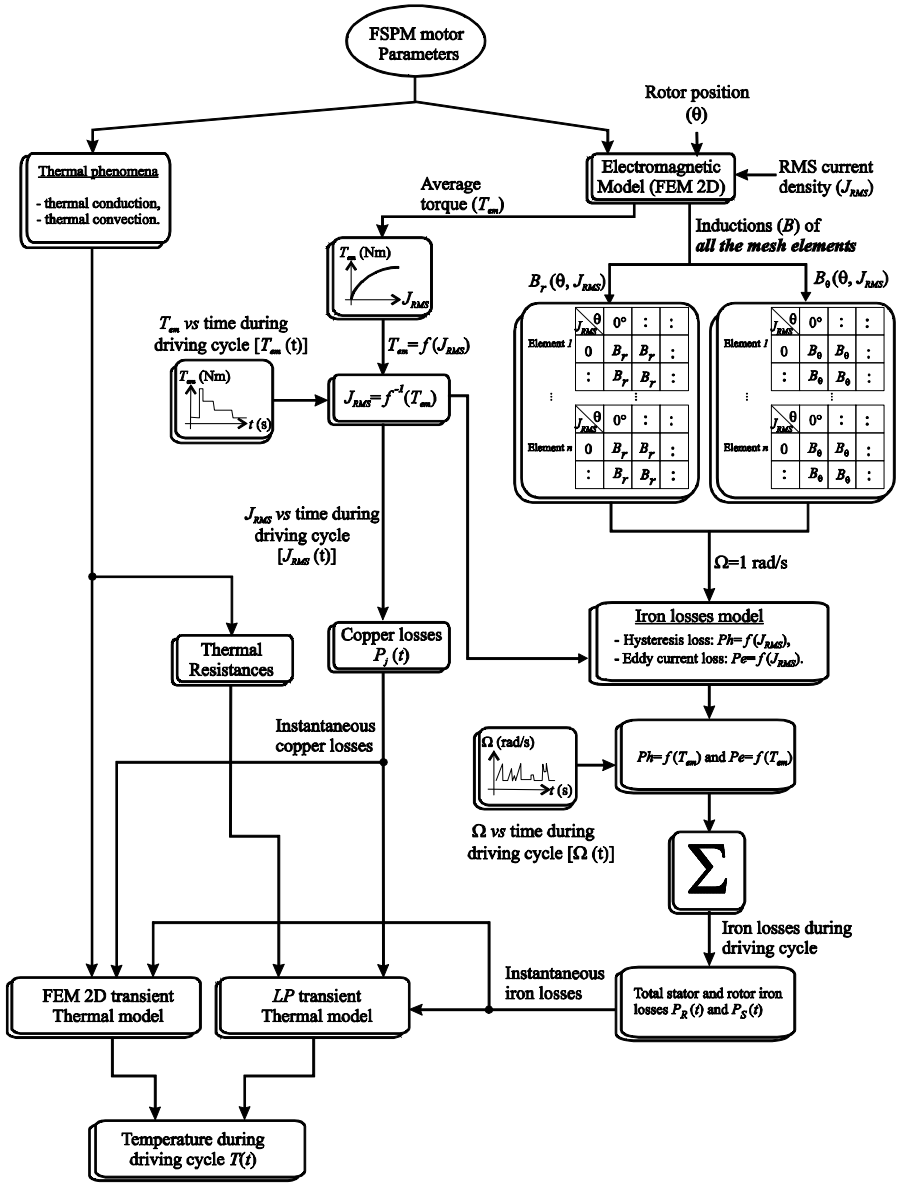

Fig. 4 Flow chart of the thermal-electromagnetic model for electrical machines with driving cycles

$$\left(\frac{\partial B}{\partial t}\right)^2 = \frac{\Delta B_r^2 + \Delta B_\theta^2}{\Delta t^2} \tag{2}$$

where Δt is time step, ΔB_r and ΔB_θ are respectively the normal and tangential components of flux densities.

The excess iron loss and the minor loop hysteresis iron loss as well as the losses in permanent magnets were not taken into account. The expression of iron losses densities [P_x (W/m^3), subscript x represents the stator or the rotor] of the rotor and the stator could be established as [26]

$$P_x(W/m^3) = f_x\left(k_{h1}\cdot \Delta B_{pp} + k_{h2}\cdot \Delta B_{pp}^2\right) + k_e f_x \int_0^{\frac{1}{f_x}} \left(\frac{\partial B}{\partial t}\right)^2 dt \tag{3}$$

where

f_x ($x = R, S$) : Rotor (R) or Stator (S) electrical frequency,

k_{h1} = 5 A/m and k_{h2} = 40 Am/Vs : Hysteresis loss coefficients,

B_{pp} ($Tesla$) : Peak-to-Peak value of flux density,

k_e=0.022 Am/V : Eddy current loss coefficient.

The hysteresis and eddy current loss coefficients are obtained from the characteristics of the laminated sheets [Fe-Co 50, see Fig. 3 (a)]. With the expression (3) and a rotor speed $\Omega = 1\mathrm{rad/s}$, the hysteresis (Ph) and eddy current losses (Pe) can be obtained for all the mesh elements of FSPM motor 12/10, which are in function with the RMS current density [$Ph=f$ (J_{RMS}), $Pe=f$ (J_{RMS})]. Knowing the relationship between the RMS current density and the average torque [$J_{RMS} = f^{-1}(T_{em})$], the analytical relationship between each element hysteresis as well as eddy current losses and the average torque can then be established [$Ph=f$ (T_{em}) and $Pe=f$ (T_{em})]. Using average torque [T_{em} (t)] and the rotor speed [Ω (t)] versus time during one driving cycle, the hysteresis and eddy current losses of each element during one driving cycle can be

obtained. Summing hysteresis and eddy current losses of all the elements of rotor as well as the stator, the total stator and the rotor iron losses versus time during one driving cycle can be finally obtained [P_R (t) and P_S (t)]. The obtained instantaneous rotor and stator iron losses as well as the instantaneous copper losses will be used as heat sources of the LP and FEM 2D transient thermal models for calculating the temperatures of different motor parts. The transient thermal models will be detailed in the following parts of this paper.

Based on the characteristic parameters and previous methods for calculating the power losses, the copper and iron losses during one driving cycle were obtained as in Fig. 5.

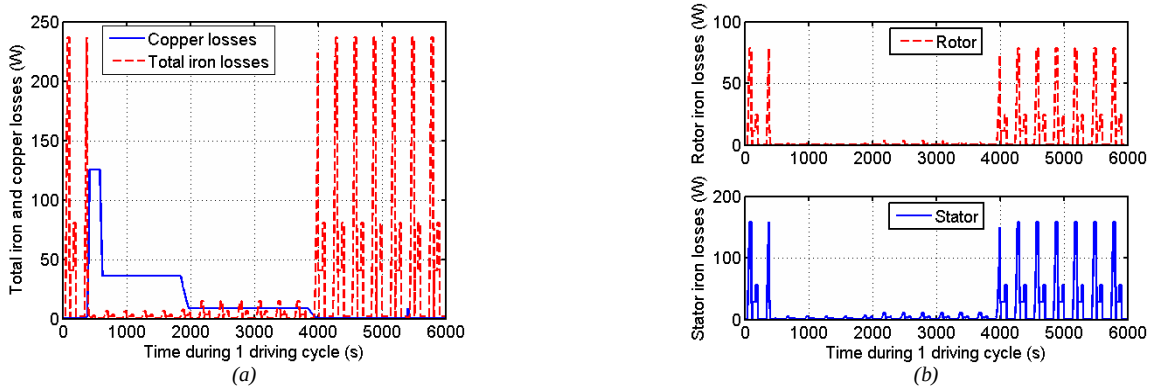

Fig. 5 Copper and total iron losses during one driving cycle of the dual star FSPM motor for VSV application.

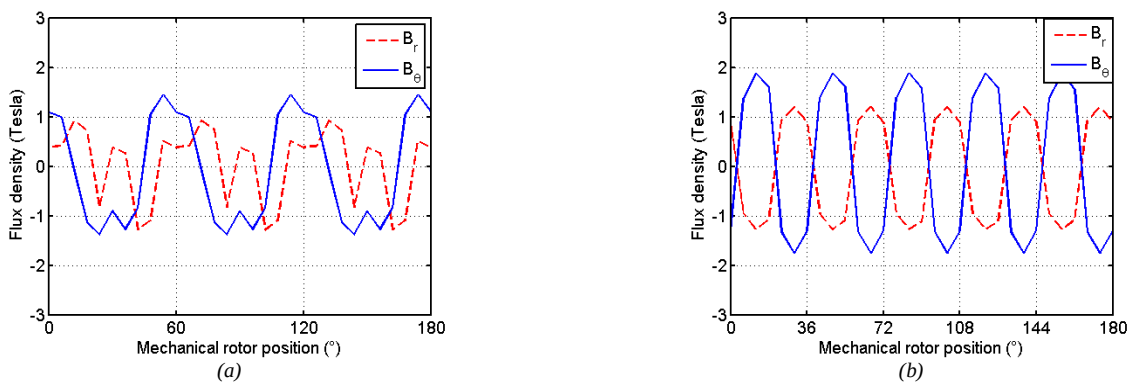

Fig. 6 Rotor and stator teeth magnetic flux density (B_r and B_θ) versus rotor position. The calculations are for 180 mechanical degrees. (a) rotor tooth, (b) stator tooth.

As been shown in Fig. 5 (a), the maximum copper losses (126 W) and minimum iron losses (0.5 W) appear from 380s to 620s, and the minimum copper loss (0.3 W) as well as maximum iron losses (245 W) appear from 0s to 360s and from 4000s to 6000s. The rotor and stator iron losses versus time during one driving cycle is shown in Fig. 5 (b). For the dual star FSPM motor in this paper, the period of rotor flux density (60 mechanical degrees) is 2 times higher than that of the stator (30 mechanical degrees) as shown in Fig. 6. However, the harmonics in the rotor flux density are also significantly higher than that of the stator. As results, even if with a lower rotor frequency, the rotor iron losses could be as high as one half of that of the stator.

IV. Transient Thermal Model of Dual Star FSPM Motor with Driving Cycle

A. *Thermal Conduction of Machine Components*

In this paper, as mentioned in previous sections, the stator structure of the dual star FSPM motor is symmetrical. Thus, the thermal studies on one part of the stator to represent the whole stator are possible [14]. The stator structure to be studied was shown in Fig. 7 (a), which is 1/12 of the whole stator. It has long been known that the maximum temperature of the machine is in the stator end-windings because in the stator slots, the axial thermal conductivity is almost the same as that of the copper, which is 350 W/m/°C, while in radial direction, due to existence of insulating materials, the equivalent thermal conductivity is significantly lower than that in axial direction. Thus, the heat generated in stator slots are removed to the end-windings and dissipated by the convection of cooling fluid nearby the end-windings [14]. However, the modeling of the convection nearby the end-windings is a challenging task, which demands experimental tests and the convection coefficient in these regions is considerably sensible to the variation of end winding structures. Thus, in the conception process as in this paper, the thermal studies were limited in the radial direction. As in most of previous thermal studies [15]-[27], the stator slots were considered as an equivalent homogeneous material, and the equivalent thermal conductivity can be obtained by analytical, Finite Element and experimental methods.

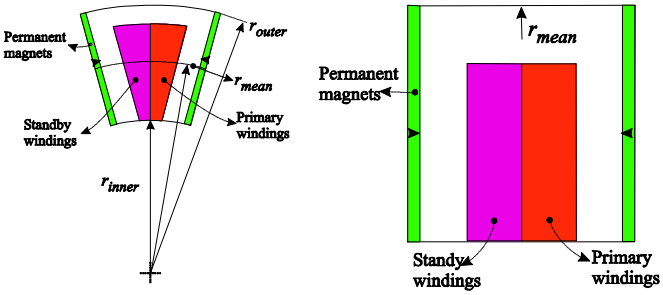

(a) (b)

Fig. 7 Transformation of the real stator structure of the dual star FSPM motor in a regular one (rectangular). (a) real cross-section of stator structure, (b) regular cross-section of stator structure.

In the electrical machines, the form of stator slots is often not regular, e.g. fan-shaped, or with round inside corners, etc, thus, in order to simplify the studies, especially for calculating the thermal resistances, it is often necessary to transform the real structure in a regular one. The transformation method in [14] was not accurate enough, which could cause significant errors in computing the maximum temperature in stator slots. In this paper, a novel transformation method was proposed and the principle of this method is shown in Fig. 7, which could simplify considerably the calculation of the thermal resistances of the machine components and, in the mean time, give a satisfactory calculate precision.

In order to realize the transformation of structure as shown in Fig. 7 and not change the physical reality, it should make sure that the area of stator slots, the widths of stator teeth as well as the permanent magnets, the stator radial length, the stack length and the stator slots filling coefficient are the same as those in real stator. The outer radius of regular stator was chosen as the mean radius r_{mean} between the outer r_{outer} and inner r_{inner} radii of real stator, the expression of which is

$$r_{mean} = \frac{r_{outer} + r_{inner}}{2} \tag{4}$$

With the (4), the area of the outer surface of the regular stator S_{outer_reg} is obtained as

$$S_{outer_reg} = 2\pi \cdot r_{mean} \cdot L \tag{5}$$

Where L is the stack length of dual star FSPM motor. After this kind of treatment, it could be noticed that the areas of stator slots, the stator core iron and the permanent magnets of the regular stator are the same as those in the real stator. Thus the iron and copper losses can be considered the same in the regular stator as those in the real stator. However, it should be noted that after the transformation, the area of outer surface of the stator was decreased from ($2\pi \cdot r_{outer} \cdot L$) to ($2\pi \cdot r_{mean} \cdot L$), since the thermal convection between the outer surface of stator and ambient environment depends on the area of outer surface of stator, and can be modeled as in (6), this would increase maximum temperature in the regular stator structure. Thus, in order to compensate the influence of the transformation on the variation of maximum temperature, a transformation coefficient should be employed, the expression of which is shown in (7).

$$R_{conv} = \frac{1}{hS_{outer}} \tag{6}$$

$$\varepsilon_{tr} = \frac{S_{outer_reg}}{S_{outer_real}} = \frac{r_{mean}}{r_{outer}} \tag{7}$$

Where R_{conv}, $h = 30\ Wm^{-2}K^{-1}$, $\varepsilon_{tr} = 0.786$ are respectively the thermal resistance due to the thermal convection between outer surface of stator and ambient environment, the thermal convection coefficient and the transformation coefficient. Finally, the thermal resistance of the real parts (R_{real}) can be obtained by the thermal resistance of equivalent regular structure (R_{reg}) as

$$R_{real} = \varepsilon_{tr} R_{reg} \tag{8}$$

With the transformation coefficient ε_{tr}, the relationship between the maximum temperature of real stator structure ($T_{\max_real}$) and that of regular stator structure ($T_{\max_reg}$) can be established such as

$$T_{\max_real} = \varepsilon_{tr}(T_{\max_reg} - T_a) + T_a \tag{9}$$

Where $T_a = 150°C$ is the ambient temperature (given in the machine specification of VSV application).

In order to verify the previous transformation method, the Finite Element Method is applied for computing the variation of steady-state temperature during one driving cycle. In this part, for simplicity, only the copper loss as shown as in Fig. 5 was taken into account. The numerical results are shown in Fig. 8, a quite good agreement between the maximum temperature of the real stator structure ($T_{\max_real}$) and that of the regular stator structure was observed.

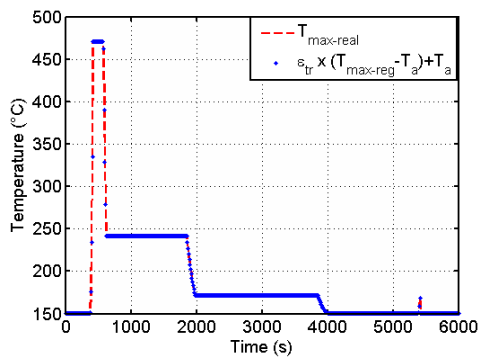

Fig. 8 The comparison of maximum temperature obtained by FEM 2D between the real stator structure and the regular stator structure

With the regular stator structure (rectangular), the thermal resistances of different materials in stator can be obtained by resolved Poisson's equation (2D rectangular) with heat sources as in the primary phase windings and stator core iron, and by resolved Laplace's equation (2D rectangular) without heat sources as in the standby phase windings and the permanent magnets (in this paper, the permanent magnets were supposed without losses). The principle equations are shown in Fig. 9 ($\Delta T = -P_j/\lambda$ for the zone *I* and $\Delta T = 0$ for the zone *II*), which was simplified to resolve 1D problem. The heat source is only in the zone *I*, the thermal flux was supposed to flow in the direction of axis *x*, and the Dirichlet boundary conditions were applied to the surface (in axis *z*)

where $x=H$ ($H=2l$, H is the length of the studied zone), on the other surfaces (in axis z), the Neumann boundary conditions were applied. In Fig. 9, λ, T_a, P_j are respectively the thermal conductivity, the ambient temperature and the power loss (heat source), while Δ is the Laplacian operator. With previous conditions, after resolving the Poisson and Laplace's equations in different zones, the thermal resistances can be obtained as follows:

$$\begin{cases} R_I = \dfrac{l}{2\lambda \cdot S} \text{ for Zone } I \\ R_{II} = \dfrac{l}{\lambda \cdot S} \text{ for Zone } II \end{cases} \tag{10}$$

Where l is the zone length in axis x, S is the area of surface of y-z axis (perpendicular to x-axis).

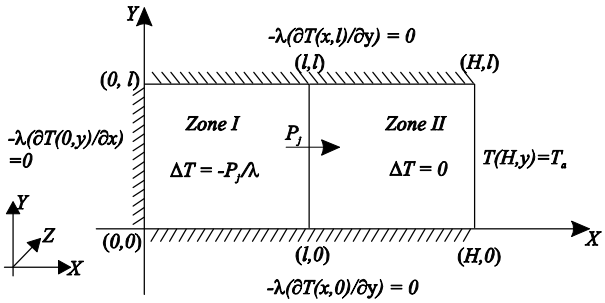

Fig. 9 Zones representing different components of machine to be studied, Zone I: with heat source ($P_j \neq 0$), Zone II: without heat source ($P_j = 0$).

B. Thermal Convection in the Air-Gap

Without motor fan on the rotor, the axial fluid flow in the air-gap could be neglected comparing to the radial fluid flow. Furthermore, even if the air flow in the air-gap is turbulent, it could still be considered that there is a thin layer of air nearby the rotor tooth tips, which is laminar, and rotates with the rotor with the same peripheral speed of rotor tip. This is the same case for the air flow inter-rotor teeth. Thus, the convection coefficient in the air-gap could then be calculated as follows [14], [27]

$$Ta = \frac{\rho^2 \cdot \Omega^2 \cdot r_a \cdot e^3}{\mu^2} \tag{11}$$

Where

Ta	:	Taylor number,
$r_a = e/\ln\left(\frac{r_{inner}}{r_{r_outer}}\right)$	:	Mean logarithmic radius,
$e\ (m)$	:	Air-gap length,
$r_{inner}\ (m)$	:	Stator inner radius (see Fig. 7),
$r_{r_outer}\ (m)$	:	Rotor outer radius.
$\mu\ (Pa \cdot s)$	:	Fluid dynamic viscosity in air-gap,
$\rho\ (kg/m^3)$	:	Density of fluid in air-gap,
$\Omega\ (rad/s)$	:	Rotor mechanical speed,

Based on the obtained Taylor number, the Nusselt number (Nu) can then be calculated as

$$\begin{cases} Nu = 2 & (Ta < 1708) \\ Nu = 0.128Ta^{0.367} & (1800 < Ta < 12000) \\ Nu = 0.409Ta^{0.241} & (12000 < Ta < 4.10^6) \end{cases} \tag{12}$$

The convection coefficient could finally be established as

$$h = \frac{Nu \cdot D_h}{\lambda} \tag{13}$$

Where D_h (m) is the hydraulic diameter, which is equal to two times the air-gap length ($2 \times e$) for the electrical machines with narrow air-gap [27].

As shown in Fig. 2, the maximum rotor velocity during the driving cycle is 8000 rpms, and with this velocity, the maximum Taylor number is about 285.8, which is less than 1708. Thus, for all the range of rotor velocities of the driving cycle, the Taylor number is always less than 1708 because the higher the rotor velocity, the higher the Taylor number. As a result, the Nusselt number and the convection coefficient in the air-gap are constant, and which are respectively equal to 2 and 150 $Wm^{-2}K^{-1}$. Finally, the thermal resistance due to thermal convection in the air-gap could be obtained using the expression (6). It should be noted that the precise computation of thermal convection coefficient is a significantly demanding task. This can be performed by lots of Computational Fluid Dynamics (CFD). While the CFD calculations are very time-consuming and need a solid knowledge of mechanical fluid in air-gap, this is certainly a very challenging task in the preliminary conception process of the electrical machines. In the accessible literature [27], an augmentation of 20% of surface exchange due to the rotor slots are reported. In this paper, the rotor iron losses are relatively low, and it is safe to use the foregoing method to calculate the thermal convection coefficient.

C. Thermal Capacitances of Machine Components

In transient thermal model, the thermal capacitance should be added to calculate the ability to store heat of each machine component. For the component where exist heat source as in the zone I shown in Fig. 9, the thermal capacitance should connect with the energy injecting node, while in the zone II (without heat source), the thermal capacitance connect with the thermal resistance. A simple example of transient thermal analysis in different study zones of the Fig. 9 can be modeled as in Fig. 10. T_I and T_{II} are the node temperatures, R_I and R_{II} are respectively the thermal resistances of the zone I and the zone II while C_I and C_{II} are the thermal capacitances, which can be calculated by (14).

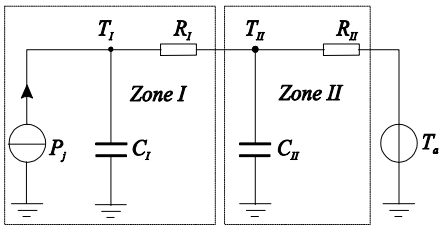

Fig. 10 Simple example of transient thermal analysis in different study zones. Zone I, with heat sources (P_j), (b) Zone II, without heat sources

The thermal capacitance [$C_{th}\ (J/°C)$] in different zones of Fig. 10 can be calculated as

$$C_{th} = c_p \cdot M = c_p \cdot V \cdot \rho \tag{14}$$

Where c_p ($J/kg/°C$), M (kg), V (m^3) and ρ (kg/m^3) are the specific heat capacity, the masse, the volume and the density, respectively.

D. Lumped Parameter Transient Thermal Model for Driving Cycle

With the given machine parameters as shown in Fig. 11 (a), the thermal resistances [see (10)] and capacitances [see (14)] of different motor components can be obtained. An example as (15) is given for calculating the thermal resistance and capacitance of the primary winding [see Fig. 11 (b)], which could be also applied for other motor components.

$$\begin{cases} R1 = \dfrac{1}{4}\dfrac{h_{winding_s}}{\lambda_{winding} \cdot l_{winding_s} \cdot L} \\ R2 = \dfrac{1}{2}\dfrac{l_{winding_s}}{\lambda_{winding} \cdot h_{winding_s} \cdot L} \end{cases} \quad \text{and} \tag{15}$$

$$C1 = \rho_{winding}\left(h_{winding_s} \cdot l_{winding_s} \cdot L\right)c_{winding}$$

where $l_{winding_s}$ and $h_{winding_s}$ are respectively the length and the height of the primary stator slot and L is the stack length of the machine, while $\lambda_{winding}$, $\rho_{winding}$ and $c_{winding}$ are respectively the equivalent thermal conductivity, the mass density and specific heat capacity of the primary stator slot.

With all the obtained thermal resistances and capacitances of different motor components, the complete Lumped Parameter (LP) transient thermal model of the dual star FSPM motor is established as shown in Fig. 11 (b). The description of different thermal resistances and capacitances is given in Table 1. P_j is the copper loss of the primary phase while P_{f1}-P_{f5} are the iron losses of different parts of stator as well as of rotor. In this paper, the distribution of copper loss and iron loss are considered as homogeneous. Generally, in order to improve the calculate accuracy, more thermal resistances should be required [14], while this would be high time consuming and could loss the advantageous of the thermal resistance network method.

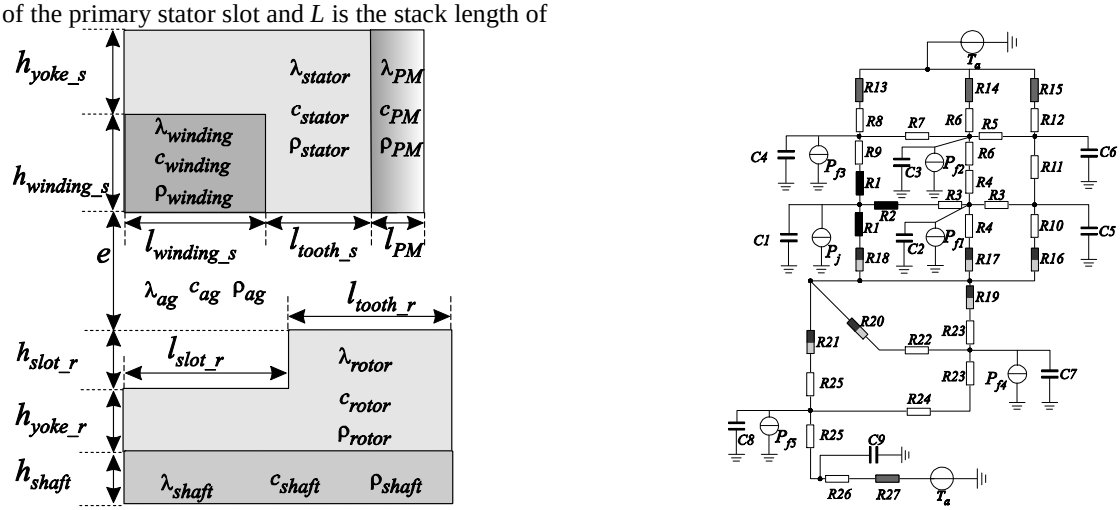

(a) machine parameters *(b) LP thermal model*

Fig. 11 Equivalent thermal resistance network of the regular stator of the dual star FSPM motor 12/10 (Lumped-Parameter Model).

Table 1 Description of thermal resistances and capacitances shown in the Fig. 11

Location	Resistance	Capacitance	Location	Resistance	Capacitance	Location	Resistance	Capacitance
Winding	*R1 – R2*	*C1*	Permanent magnet	*R10 – R12*	*C5 – C6*	Rotor	*R22 – R25*	*C7 – C8*
Stator tooth	*R3 – R4*	*C2*	Outer convection	*R13 – R15,R27*	–	Shaft	*R26*	*C9*
Stator yoke	*R5 – R9*	*C3 – C4*	Air-gap convection	*R16 – R21*	–			
R16-R21 in the air-gap is due to the conducto-convection of fluid.								

Based on the thermal network shown in Fig. 11 (b), a relationship among the thermal conductance, thermal capacitances, the node temperature and the node power losses can be finally established as follows:

$$[C]_{n\times n}\frac{d[T]_{n\times 1}}{dt} + [G]_{n\times n}[T]_{n\times 1} = [P]_{n\times 1} \tag{16}$$

$[C]_{n\times n}$ is the thermal capacitance matrix, $[T]_{n\times 1}$ is the node temperature matrix, $[P]_{n\times 1}$ is the node power loss matrix, $[G]_{n\times n}$ is the thermal conductance matrix, the diagonal component of which is the self conductance of the node i, which is the sum of all the thermal conductances connected with this node. Whereas, in the upper as well as in the lower triangular components (G_{ij} with $i \neq j$), which are mutual conductances and equal to negative conductances connected the node i and the node j. If there is no direct connection between the nodes, which is often the case in thermal network of electrical machines, the thermal conductances are null. Based on (16), the temperature variation in the simple example as shown in Fig. 10 could be calculated as

$$\underbrace{\begin{bmatrix} C_I & 0 \\ 0 & C_{II} \end{bmatrix}}_{[C]}\frac{d}{dt}\underbrace{\begin{bmatrix} T_I \\ T_{II} \end{bmatrix}}_{[T]} + \underbrace{\begin{bmatrix} \frac{1}{R_I} & -\frac{1}{R_I} \\ -\frac{1}{R_I} & \frac{1}{R_I}+\frac{1}{R_{II}} \end{bmatrix}}_{[G]}\begin{bmatrix} T_I \\ T_{II} \end{bmatrix} = \underbrace{\begin{bmatrix} P_j \\ 0 \end{bmatrix}}_{[P]} \tag{17}$$

E. FEM 2D Transient Thermal Model for Driving Cycle

Different from the non-salient electrical machines, the FEM 2D transient thermal model at one rotor position is not suitable

for the doubly salient machine in this paper. However, it is always possible to transform the salient rotor into a non-salient one. As we know that the thermal time constant is much longer than the mechanical period of dual star FSPM motor, thus, the air at the middle of air-gap could be considered heated up uniformly by the rotor tooth tip or the inter-rotor teeth air. As a result, it could be considered that the air layer in the middle of air-gap is isothermal. Moreover, due to the viscosity of air in the air-gap, there is a thin layer of air (all the temperature drop of air-gap is in this thin layer) nearby the rotor tooth tip rotates with the rotor with the same peripheral velocity [28]. Thus, to the immobile part of stator, the rotating rotor part (the mobile rotor and the half of air-gap nearby the rotor) could be considered as an equivalent homogeneous material and which is immobile. The equivalent radial thermal resistance of the rotor could be obtained using the method shown in Fig. 12.

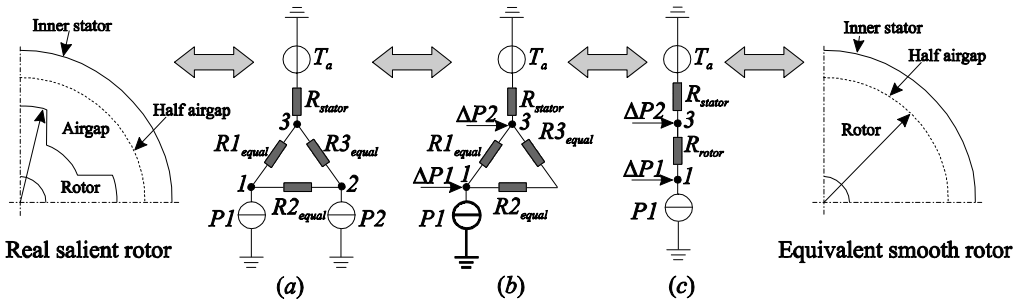

Fig. 12 Procedure of calculating the equivalent rotor thermal resistance of the dual star FSPM motor.

In Fig. 12, for simplicity, the stator part (stator and the stator half air-gap) is represented by only one thermal resistance (R_{stator}). T_a (150°C in this paper) is the ambient temperature, $P1$ and $P2$ are respectively the iron losses P_{fr5} and P_{fr4} in the rotor. The different components in Fig. 12 (a) and (b) can be obtained using the network of Fig. 11 (b) as

$$\begin{cases} R1_{equal} = R21 + R25 \\ R2_{equal} = R23 + R24 \\ R3_{equal} = \dfrac{(R20 + R22)\cdot(R19 + R23)}{R20 + R22 + R19 + R23} \end{cases} \tag{18}$$

$$\begin{cases} \Delta P1 = R3_{equal}\cdot P2/(R2_{equal} + R3_{equal}) \\ \Delta P2 = R2_{equal}\cdot P2/(R2_{equal} + R3_{equal}) \end{cases} \tag{19}$$

The rotor part equivalent thermal resistance (R_{rotor}) in Fig. 12 (c) could then be obtained as

$$R_{rotor} = \frac{(R3_{equal}+R2_{equal})\cdot R1_{equal}}{(R1_{equal} + R2_{equal} + R3_{equal})} \tag{20}$$

Based on (10), the equivalent radial thermal conductivity (λ_{equal}) of the equivalent rotor could be finally obtained.

Concerning the equivalent mass density (ρ_{equal}) and equivalent specific heat capacity (c_{equal}) of rotating rotor part, which can be calculated as follows

$$\begin{cases} \rho_{equal} = \dfrac{V_{rotor}\cdot\rho_{rotor}}{V_{equal}} \\ c_{equal} = \dfrac{V_{rotor}\cdot\rho_{rotor}\cdot c_{rotor}}{V_{equal}\cdot\rho_{equal}} \end{cases} \tag{21}$$

where V_{rotor}, ρ_{rotor} and c_{rotor} are respectively the volumes, the mass densities and the specific heat capacities of rotor iron. Due to its low mass density, the mass and thermal capacitance of the air in air-gap are neglected.

With the obtained equivalent parameters, the FEM 2D transient thermal model of the dual star FSPM motor can be established and its boundary conditions are shown in Fig. 13. The copper (P_j) and stator iron losses (P_f) are homogeneously distributed in the primary winding and the stator teeth and yoke, respectively. In the permanent magnets and the redundant winding as well as the shaft, no power losses exist. For modelling the half stator air-gap, where the thermal conducto-convection exists, an equivalent thermal conducivity (λ_{ag_equal}) is applied and, the thermal resistance obtained by using λ_{ag_equal} is equal to the conducto-convective thermal resistance in the half stator air-gap. $P1 + \Delta P1$ is the equivalent iron loss in the equivalent rotor while $\Delta P2$ is the iron losses injected through the line of the rotor outer surface into the air-gap.

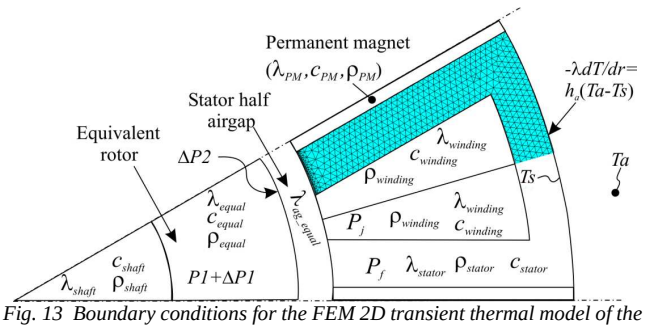

Fig. 13 Boundary conditions for the FEM 2D transient thermal model of the dual star FSPM motor.

F. Analytical and Numerical Results of Variation of Temperature for Driving Cycle

With the LP transient thermal model and the FEM 2D transient thermal model shown in Fig. 11 (b) and Fig. 13, the computation of temperature variation versus time during driving cycles could be finally performed. The analytical and numerical results of temperature variation during 4 cycles (the machine reaches the permanent regime) are shown in Fig. 14. A good agreement between the results obtained by LP model and that obtained by FEM was observed. In Fig. 14 (a), the heat sources are the average copper loss (14.9 W), the stator average iron losses (14.6 W) as well as the rotor average iron losses (6.34 W), while in Fig. 14 (b), the heat sources are instantaneous copper and iron losses during driving cycles. It is important to find that the maximum temperature by obtained

using average losses is much lower than that obtained by using instantaneous losses. Thus, the transient thermal model using the instantaneous power losses as heat source is essential for evaluating the real thermal performance of the electrical machines with driving cycles. Otherwise, the thermal performance of the machine could be overestimated.

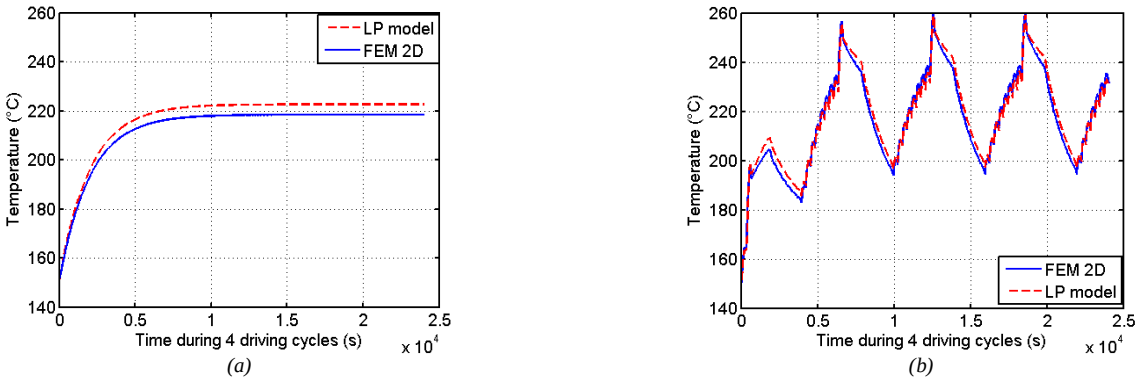

Fig. 14 Variation of temperature in primary winding of dual star FSPM motor during 4 cycles (the machine reaches the permanent regime). The results are obtained by LP model as well as by FEM 2D. (a) heat source is the average copper and iron losses during one driving cycle. (b) heat sources are the instantaneous copper and iron losses.

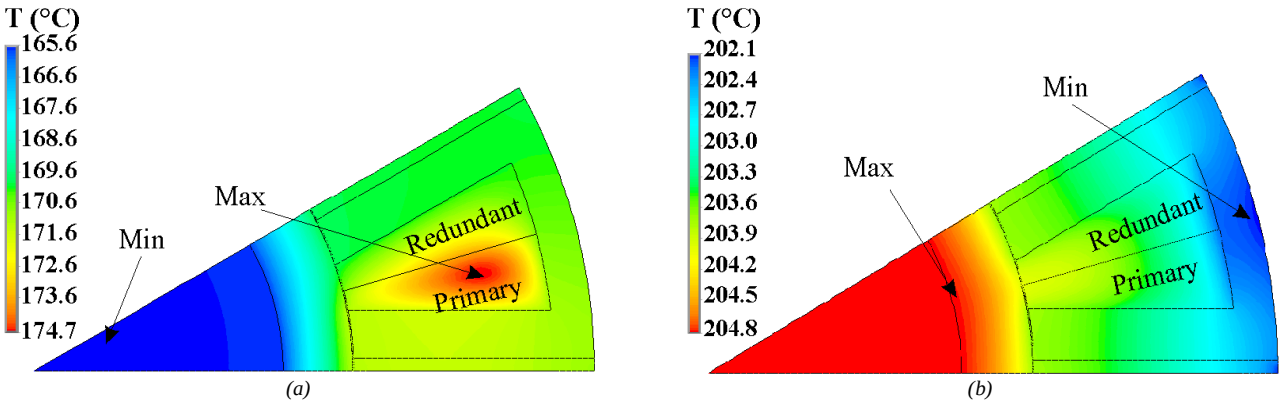

Fig. 15 Temperature distribution of FSPM motor with primary phase supplied at different moments during driving cycle. (a) at 600 seconds, (b) at 4300 seconds.

It should be noted that the maximum temperature in Fig. 14 (b) is slightly high that will cause some thermal problem for the isolation in primary phase winding (the isolations is class C, the admissible maximum temperature is about T_{max} = 240°C). In order to decrease the maximum temperature, the minimisation of the power losses is always a good choice while enhancing the performance of cooling system is also a good alternative. The rotor mounted fan (Totally Enclosed Fan Cooled (TEFC) structure) could be applied to increase the air circulation and the axial fluid flow in the air-gap. While on external surface of the frame, several kinds of cooling fins could be applied to increase the heat exchange area, etc.

It was also found that the maximum temperature can move from the primary winding to other parts as shown in Fig. 15, in which the temperature of rotor can be slightly higher than that of the primary winding. This is because that the iron losses could be sometimes significantly higher than copper loss. Furthermore, the air-gap is not a good thermal conductor even with the forced convection for a doubly salient motor structure as in this paper. Thus during one driving cycle, the maximum temperature point could move from stator slots to rotor yoke or elsewhere, e.g. at 600 seconds, the maximum temperature was observed in the primary and its value is about 174.7 °C, while at 4300 seconds, a maximum temperature of 204.8 °C was observed at the rotor yoke.

G. *Experimental Verification*

In order to verify the results obtained by the analytical and numerical models, a 12-slot and 10-pole flux switching permanent magnet motor (FSPM) is used (see Fig. 16), in which the stator and rotor outer diameters are respectively 154.4 mm and 86 mm, the air-gap length is 0.2 mm, the stack length is 60mm while the frame length is 105 mm, and the filling factor is 0.4. The FSPM motor is driven by a DC machine, the speed of which is $\Omega = 270\ \mathrm{tr/min}$. The no-load Electromotive Force (EMF) of the primary phase A1 is calculated by the FEM 2D as in the previous sections. This is validated by the experimental tests as shown in Fig. 17.

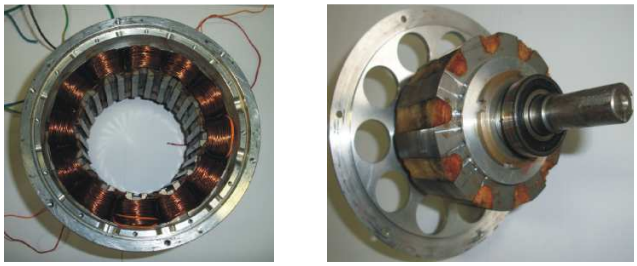

(a) Stator *(b) Rotor*

Fig. 16 Prototype of a dual star FSPM motor (12/10).

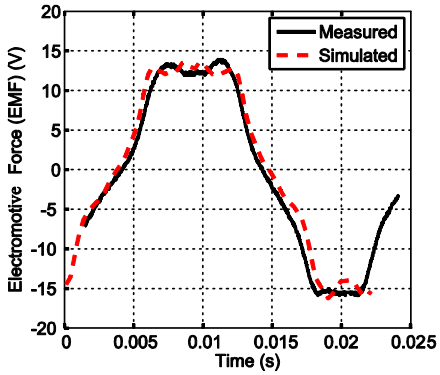

Fig. 17 Simulated and measured Electromotive Force for one period of a dual star FSPM motor (12/10)

In order to measure the temperature of the FSPM motor, two thermal sensors are respectively implemented in the middle of the stator slot and on the outer surface of the machine. The first one is to measure the maximum temperature of the stator slot while the second one is to measure the outer surface temperature, which will allow us to calculate the outer surface thermal convection coefficient. In laboratory conditions, the natural thermal convection coefficient is about $h = 4\,W/m^2/°C$ and for a filling factor of 0.4, the equivalent thermal conductivity in the stator slots is about $\lambda = 0.25\,W/m/°C$. As shown in Fig. 14, two cases are dealt with in this part: in Fig. 18 (a), the power losses are constant, the value of which is 68.5 W. While in Fig. 18 (b), the power losses are variables, from 0 seconds to 3600 seconds, the power losses are constant and equal to 91.3 W, after 3600 seconds, the supply of the machine is turned off until 5400 seconds, and then the machine is supplied with constant power losses of 91.3 W (the average power loss is equal to 68.5 W). A good agreement is observed between the analytical results obtained by the LP model and the experimental results. The difference between the measured and simulated results is mainly due to the neglect of the contact thermal conductivity between the machine components, the neglect of the thermal radiation on the outer surface of the machine and the roughly estimated thermal convection coefficient in the air-gap, etc.

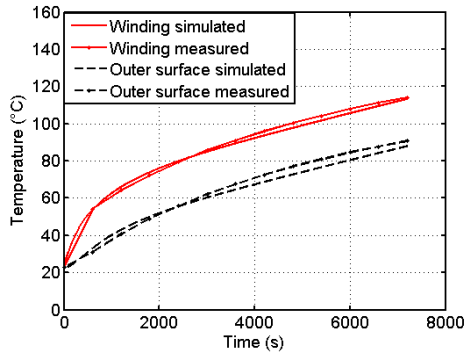

(a)

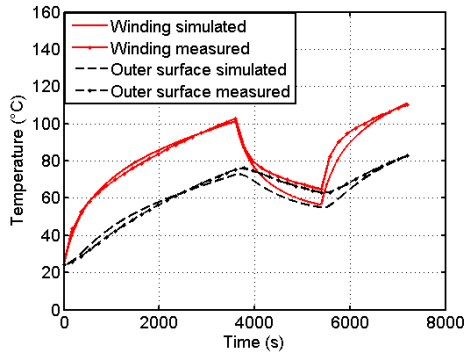

(b)

Fig. 18 Variations of temperature of windings and the outer surface obtained by simulation and validated by experimental method. (a) the power losses are constant, (b) the power losses are variable.

V. Conclusion

The copper and iron loss model of a dual star (2 × 3 phase) FSPM motor with driving cycles have been performed in this paper, the results of iron and copper losses during driving cycles showed that at high rotor velocities, the iron losses are significantly higher than copper loss while this is inverse at high output torques.

In order to calculate the temperature variation of the dual star FSPM motor, a Lumped Parameter (LP) and a Finite Element Method (FEM) 2D transient thermal model for driving cycles have been carried out. Since the power losses are not constant during a driving cycle, the temperature changes also in function with time for a driving cycle. It is found that the maximum temperature obtained by instantaneous power losses (heat sources) is much higher than that obtained by average losses of a driving cycle. Moreover, with instantaneous power losses as heat sources, the maximum temperature can move from stator slots to the rotor yoke. Thus, the transient thermal model with instantaneous power losses as heat sources is essential to predict the temperature variations for electrical machines with driving cycles. Otherwise, the thermal performance could be overestimated.

The results obtained by the FEM method and the LP model are finally validated by the experimental tests. The electromagnetic-thermal model for driving cycle can be extended for other applications with driving cycles. With the axial thermal conductivity of different motor components, the FEM 2D transient thermal model for driving cycles could also be developed for covering the 3D thermal problems.

APPENDIX
STRUCTURAL DATA FOR FSPM MOTOR

Number of stator/rotor poles	12/10;
Stack length	60 mm;
Stator outer radius	45 mm;
Rotor outer radius	25.5 mm;
Air-gap length	0.2 mm;
Shaft radius	20 mm;
Filling factor	0.5;
Permanent magnet length	2 mm;
Copper resistivity (200 °C)	$3\ 10^{-8}\ \Omega$m.

THERMAL DATA FOR FSPM MOTOR

	Conductivity (W/m/°C)	Density (kg/m3)	Specific heat capacity (J/kg/°C)
Iron (Fe-Co 50)	30	8150	460
Equivalent windings	0.84	6380	487.2
Air	0.03	1.23	1005
Permanent magnet	4	5990	450
shaft	55	7700	515

REFERENCES

[1] W. Hua, M. Cheng, Z. Q. Zhu, and D. Howe , "Analysis and optimization of back emf waveform of a flux-switching permanent magnet motor," *IEEE Trans. Energy Convers.*, vol. 23, no. 3, p. 723–733, Sep. 2008.

[2] Z. Q. Zhu and D.Howe, "Electrical Machines and Drives for Electric, Hybrid, and Fuel Cell Vehicles," *Proc. IEEE*, vol. 95, no. 4, pp. 746-765, Apr. 2007.

[3] J. T. Chen and Z. Q. Zhu, "Winding Configurations and Optimal Stator and Rotor Pole Combination of Flux-Switching PM Brushless AC Machines," *to be published in IEEE Trans. Energy Convers.*

[4] Z. Q. Zhu, Y. Pang, D. Howe, S. Iwasaki, R. Deodhar, and A. Pride, "Analysis of electromagnetic performance of flux-switching permanent magnet machines by non-linear adaptive lumped parameter magnetic circuit model," *IEEE Trans. on Magn.*, vol. 41, no. 11, p. 4277–4287, Nov. 2005.

[5] E. Hoang, A. H. Ben-Ahmed, and J. Lucidarme, "Switching flux permanent magnet polyphased synchronous machines," in *in Proc. 7th Eur. Conf. Power Electron. Appl.*, 1997, p. 903–908.

[6] Y. Chen, Z. Q. Zhu, D. Howe, and Y. Y.Ye, "Starting torque of single-phase flux-switching permanent magnet motor," *IEEE Trans. on Magn.*, vol. 42, no. 10, p. 3416–3418, Oct. 2006.

[7] X. Ojeda, G. J. Li, and M. Gabsi, "Fault Diagnosis using Vibration Measurements of a Flux-switching Permanent Magnet Motor," in *IEEE-ISIE*, Bari, Italy, 4-7 July, 2010.

[8] E. Hoang, M. Lecrivain, and M. Gabsi, "3-D thermal model of an hybrid excitation flux switching synchronous machine using a 2-D FE method software," in *2010 International Symposium on Power Electronics Electrical Drives Automation and Motion (SPEEDAM)*, 14-16 June 2010, pp. 101-104.

[9] J. Lucidarme, A. Ben Ahmed, M. Gabsi, B. Multon, E. Santander, E. Hoang, and M. Lecrivain , "Improved Electrical Machine with Double Excitation," patent WO/1998/048502, Oct. 29, 1998.

[10] N. Takorabet, J. P. Caron, B. Vaseghi, B. Nahid-Mobarakeh, F. Meibody-Tabar, and G. Humbert, "Study of Different Architectures of Fault Tolerant Actuator Using a Double-Star PM Motor," in *IEEE Industry Applications Society Annual Meeting, 2008. IAS'08*, 2008.

[11] M.-A. Shamsi-Nejad, B. Nahid-Mobarakeh, and S. Pierfederici, "Fault tolerant and minimum loss control of double- star synchronous," *IEEE Trans. Ind. Electron.*, vol. 55, no. 5, p. 1956–1965, may 2008.

[12] D. Ishak, Z. Q. Zhu, and D. Howe, "Comparison of PM brushless motors, with either all or alternative wound teeth," *IEEE Trans. Energy Convers.*, vol. 21, no. 1, p. 95–103, Mar. 2006.

[13] P. K. Vong and D. Rodger, "Coupled Electromagnetic–Thermal Modeling of Electrical Machines," *IEEE Trans. on Magn.*, vol. 39, no. 3, pp. 1614-1617, May 2003.

[14] J. Nerg, M. Rilla, and J. Pyrhönen, "Thermal Analysis of Radial-Flux Electrical Machines With a High Power Density," *IEEE Trans. Ind. Electron.*, vol. 55, no. 10, pp. 3543-3554, OCT. 2008.

[15] A. M. EL-Refaie, N. C. Harris, T. M. Jahns, and K. M. Rahman, "Thermal Analysis of Multibarrier Interior PM Synchronous Machine Using Lumped Parameter Model," *IEEE Trans. Energy Convers.*, vol. 19, no. 2, pp. 303-309, June 2004.

[16] A. Boglietti, A. Cavagnino, D. Staton, M. Shanel, M. Mueller, and C. Mejuto, "Evolution and Modern Approaches for Thermal Analysis of Electrical Machines," *IEEE Trans. Ind. Electron*, vol. 56, no. 3, pp. 871-882, Mar. 2009.

[17] M. A. Valenzuela and J. A. Tapia, "Heat transfer and thermal design of finned frames for TEFC variable-speed motors," *IEEE Trans. Ind. Electron.*, vol. 55, no. 10, p. 3500–3508, Oct. 2008.

[18] C. Micallef, S. J. Pickering, K. A. Simmons, and K. J. Bradley, "Improved cooling in the end region of a strip-wound totally enclosed fan-cooled induction electric machine," *IEEE Trans. Ind. Electron.*, vol. 55, no. 10, p. 3517–3524, Oct. 2008.

[19] D. G. Dorrell, "Combined Thermal and Electromagnetic Analysis of Permanent-Magnet and Induction Machines to Aid Calculation," *IEEE Trans. Ind. Electron.*, vol. 55, no. 10, pp. 3566-3574, Oct. 2008.

[20] K. N. Srinivas and R. Arumugam, "Analysis and Characterization of Switched Reluctance Motors: Part II—Flow, Thermal, and Vibration Analyses," *IEEE Trans. on Magn.*, vol. 41, no. 4, pp. 1321-1332, Apr. 2005.

[21] L. Alberti and N. Bianchi, "A Coupled Thermal–Electromagnetic Analysis for a Rapid and Accurate Prediction of IM Performance," *IEEE Trans. Ind. Electron.*, vol. 55, no. 10, pp. 3575-3582, Oct. 2008.

[22] M. F. Momen and I. Husain, "Design and Performance Analysis of a Switched Reluctance Motor for Low Duty Cycle Operation," *IEEE Trans. Ind. Appl.*, vol. 41, no. 6, pp. 1612-1618, Sep./Oct. 2005.

[23] C. Liu, K. T. Chau, W. Li, and C. Yu, "Efficiency Optimization of a Permanent-Magnet Hybrid Brushless Machine Using DC Field Current Control," *IEEE Trans. on Magn.*, vol. 45, no. 10, pp. 4652-4655, Oct. 2009.

[24] J. H. Seo, T. K. Chung, C. G. Lee, S. Y. Jung, and H. K. Jung, "Harmonic Iron Loss Analysis of Electrical Machines for High-Speed Operation Considering Driving Condition," *IEEE Trans.on Magn.*, vol. 45, no. 10, pp. 4656-4659, Oct. 2009.

[25] N. Sadowski, M. Lajoie-Mazenc, J. P. A. Bastos, M. V. Ferreira da Luz, and P. Kuo-Peng, "Evaluation and Analysis of Iron Losses in Electrical. Machines Using the Rain-Flow Method," *IEEE Trans. on Magn.*, vol. 36, no. 4, pp. 1923-1926, july 2008.

[26] D. M. Ionel, M. Popescu, M. I. McGilp, T. J. E. Miller, S. J. Dellinger and R. J. Heideman , "Computation of Core Losses in Electrical Machines Using Improved Models for Laminated Steel," *IEEE Trans. Ind. Appl.*, vol. 43, no. 6, pp. 1554-1564, Nov./Dec. 2007.

[27] J. F. Trigeol, Y. Bertin, and P. Lagonotte, "Thermal Modeling of an Induction Machine Through the Association of Two Numerical Approaches," *IEEE Trans. Energy Convers.*, vol. 21, no. 2, pp. 314-323, June 2006.

[28] G.-I. Taylor, "Stability of a viscous liquid contained between two rotating cylinders," *Philosophy Trans. Roy. Soc. London*, p. 223–289, 1923.